THE JOURNAL OF PHYSICAL CHEMISTRY C
A JOURNAL OF THE AMERICAN CHEMICAL SOCIETY

pubs.acs.org/JPCC Article

Twist-Engineered Switching of Magnetic Phase and Anisotropy in Bilayer CrSBr: A First-Principles Study

Fangyu Zhang, Zihao Xu, Diancong Qi, Weiyi Wang, Xingxing Li, Ya Su, Wujun Shi, and Zhaoyong Guan*

Cite This: https://doi.org/10.1021/acs.jpcc.5c04752 Read Online

ABSTRACT: Twist engineering of van der Waals magnets offers unprecedented opportunities to manipulate interlayer quantum states, but its impact on the magnetism of semiconductors remains poorly understood theoretically. Here, we take the CrSBr bilayer (BL) as an example to explore the influence of the twist angle (θ) on interlayer coupling, magnetism, and electronic properties. The result shows that θ weakens the dependence of interlayer interaction on the stacking modes and stabilizes ferromagnetic (FM) order regardless of the stacking modes, suppressing the intrinsic stacking-dependent antiferromagnetic (AFM) phase of pristine BL. Additionally, the direction of the easy axis (EA) undergoes multiple conversions as θ increases. The Br atomic p orbitals dominate the perpendicular magnetic anisotropy (PMA) contribution, showing a 200% enhancement at 90° twist structure versus pristine BL. Moreover, the θ transform CrSBr BL from a spin-unpolarized semiconductor into a half-semiconductor, while different θ provide additional influence on the bandgap. This work not only establishes θ as a powerful tool for controlling magnetic and electronic states in vdW semiconductors but also provides design principles for developing twist-tunable spintronic devices based on atomically thin magnets.

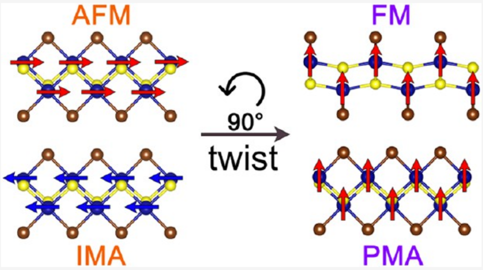

■ INTRODUCTION

Twistronics has emerged as a forefront research field in recent years due to its unique physical properties. By engineering interlayer coupling and moiré periodic potential through twist control, this approach enables precise modulation of two-dimensional (2D) material properties. Following the theoretical prediction of "magic-angle", where interlayer interaction suppressed linear momentum dispersion to create flat bands,[1] the experimental realization in twisted bilayer (BL) graphene (TBLG) via the "tear-and-stack" technique revealed extraordinary phenomena, including superconductivity,[2] van Hove singularities.[3] Subsequent studies on twisted graphene/h-BN heterostructures,[4] TBLG,[5] and twisted trilayer graphene[6] further demonstrated orbital magnetism,[4] quantum anomalous Hall effect,[7] nematic phases,[8] and reentrant superconductivity,[9] collectively establishing twistronics as a revolutionary paradigm for quantum state manipulation.[10−15]

The exploration has extended to transition metal dichalcogenides (TMDs), where twisted bilayers exhibit robust flat bands across wide angular ranges.[16] Similar to graphene, twisted BL TMDs display Mott-like insulating states,[17] topological insulating phases,[18] and even superconductivity,[19] conclusively proving that twist can fundamentally reconstruct electronic band structure.[20,21] These breakthroughs highlight the immense potential of twistronics for engineering exotic quantum states, opening new dimensions in 2D material research. Twist engineering modifies magnetic properties by creating moiré superlattices that alter interlayer coupling.[22−35] In twisted BL CrI$_3$, while the pristine system shows interlayer antiferromagnetic (AFM) order, twist induces coexisting ferromagnetic (FM) and AFM domains through competition between interlayer exchange and FM−AFM domain wall formation.[22] Direct observation of twist-induced domain wall structure has been achieved in the twisted CrI$_3$ system,[23] and the magnetic order exhibits θ-dependent configuration. Nonvolatile spin textures in these systems could be manipulated and read out via a magnetic field, where an in-plane field could induce a switch between out-of-plane and in-plane magnetic domain orientation.[36] Similar spin regulation has also been found in the twist double BL CrI$_3$ twist structure.[25] This twist-tunable magnetism extends to other van der Waals (vdW) magnets: α-RuCl$_3$ BLs[26] and CrBr$_3$ heterostructures[27] present moiré-modulated magnetic orders. Pressure-induced AFM phase transition in twisted BL 1T-VS$_2$/VSe$_2$ occurs at significantly reduced critical pressures, compared to their nontwisted counterparts.[28] Twist control in VOBr and Ca(CoN)$_2$ induces altermagnetism with spin Hall angles surpassing experimental benchmarks,[29] while MnPSe$_3$ and MnSe BLs exhibit *i*-wave spin−orbit coupled altermag-

Received: July 9, 2025
Revised: August 20, 2025
Accepted: August 27, 2025

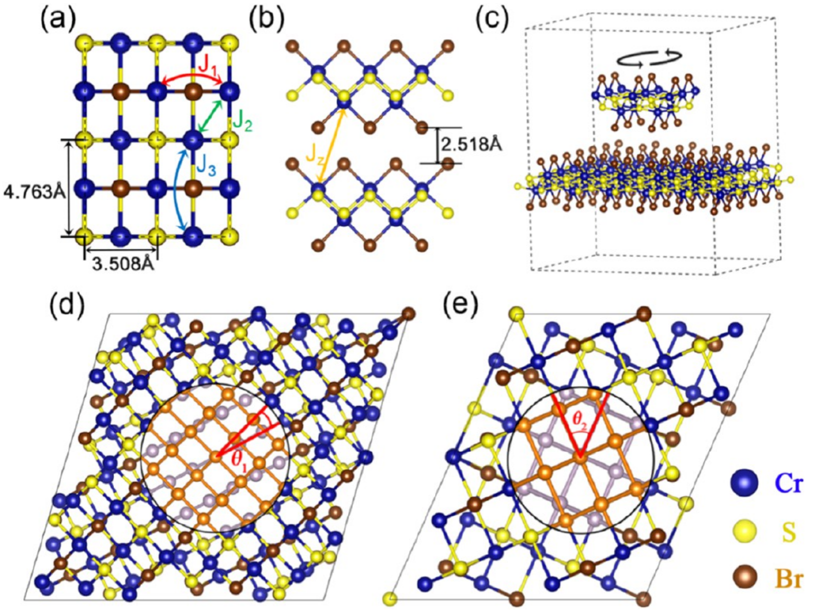

Figure 1. Illustration of the pristine BL CrSBr structure of (a) top and (b) side views. (c) Schematic diagram of the TBLC structure. Top view of the TBLC structure with θ of (d) 17° and (e) 48°.

netism under twisting.[30] Interlayer sliding in twisted BL CrX_2 (X = Se, Te) enables reversible FM−AFM switching.[31]

In recent years, the vdW magnetic semiconductor chromium bromide (CrSBr) has emerged as a compelling candidate for exploring low-dimensional magnetism and spintronic applications.[37−40] CrSBr exhibits exceptional air stability and could be readily exfoliated down to the monolayer (ML) limit, and it is predicted to maintain a high Curie temperature (T_c) (∼170 K),[41,42] significantly surpassing those of conventional 2D magnets like CrI_3 (∼45 K)[43] and $Cr_2Ge_2Te_6$ (∼25 K).[44] Another hallmark of CrSBr is its unique triaxial magnetic anisotropy,[42,45] which is enhanced by spin−orbit coupling of bromide ions, characterized by an easy axis (EA) (**b**-axis), intermediate axis (**a**-axis), and hard axis (**c**-axis). In recent years, researchers have attempted to modulate the properties of CrSBr by various methods. For instance, the application of an external electric field can induce half-metallicity in ML CrSBr,[46] while strain engineering enables effective modulation of both its magnetic phase and anisotropy.[47] In the $MoSe_2$/CrSBr heterostructure, defect-localized excitons emerge with magnetic-field-tunable valley polarization and strongly anisotropic optical responses,[48] demonstrating the unique magnetism of CrSBr can control exciton behavior. The CrSBr/GeS multiferroic heterostructures enable effective enhancement of T_c in the ferromagnetic CrSBr layer.[49] Beyond these approaches, orthogonal stacking (90°) of ML CrSBr introduces competition of interlayer magnetic anisotropies, leading to multistep magnetization switch and nonvolatile magnetic hysteresis at zero field in twisted CrSBr.[32,50] Such twisted configuration further exhibits a colossal tunneling magnetoresistance (TMR) exceeding 700%,[51] with enhanced temperature stability compared to conventional aligned stackings. These findings highlight the potential of CrSBr twistronics for the design of novel spin-based memory devices. However, experimental investigation on twisted BL CrSBr (TBLC) is still in its infancy, and theoretical predictions remain scarce.[52]

Inspired by the exotic magnetism in orthogonally stacked TBLC, this work systematically explores the interlayer interaction, magnetic order, magnetic anisotropy, and electronic properties of TBLCs at various twist angles (θ). By developing a generalized supercell construction method for orthorhombic lattices, we systematically analyze seven θ (0°−90°) with four stacking modes per angle. Our results prove that the interlayer coupling in pristine BL CrSBr exhibits strong stacking-mode dependence. However, the introduction of θ significantly reduces this stacking sensitivity while stabilizing robust FM coupling across all configurations. Furthermore, the direction of EA switches multiple times between the in-plane and out-of-plane with increasing θ. Orbital-resolved analysis identifies that Br atomic p orbitals dominate the perpendicular magnetic anisotropy (PMA), with their contribution enhanced by 200% with θ of 90°, compared to pristine BL. Additionally, the modulation of bandgap (0.66−0.84 eV) and layer-selective carrier distribution show the θ-dependent behavior, suggesting potential application in the excitonic devices.[53] This work establishes CrSBr as a prototypical system for moiré magnetism in anisotropic materials, offering a universal framework for manipulating magnetic semiconductors via twist.

■ METHODS

We conducted first-principles calculation within the framework of density functional theory (DFT) using the Vienna ab initio simulation package (VASP).[54,55] The exchange−correlation potential was treated with the Perdew−Burke−Ernzerhof (PBE) functional under the generalized gradient approximation (GGA).[56] To address the strong electron correlation effect in Cr 3d orbitals, the GGA + U method was employed with Coulomb (U = 3.30 eV) and exchange (J = 0.30 eV) parameters, yielding an effective Hubbard correction $U_{\mathrm{eff}} = U - J = 3.00$ eV, a widely used value for CrSBr.[57−59] This approach was applied to geometry optimization, electronic structure calculation, and phonon spectrum calculation. The vdW interaction was modeled through the DFT−D3 dispersion correction method.[60] The spin−orbital coupling

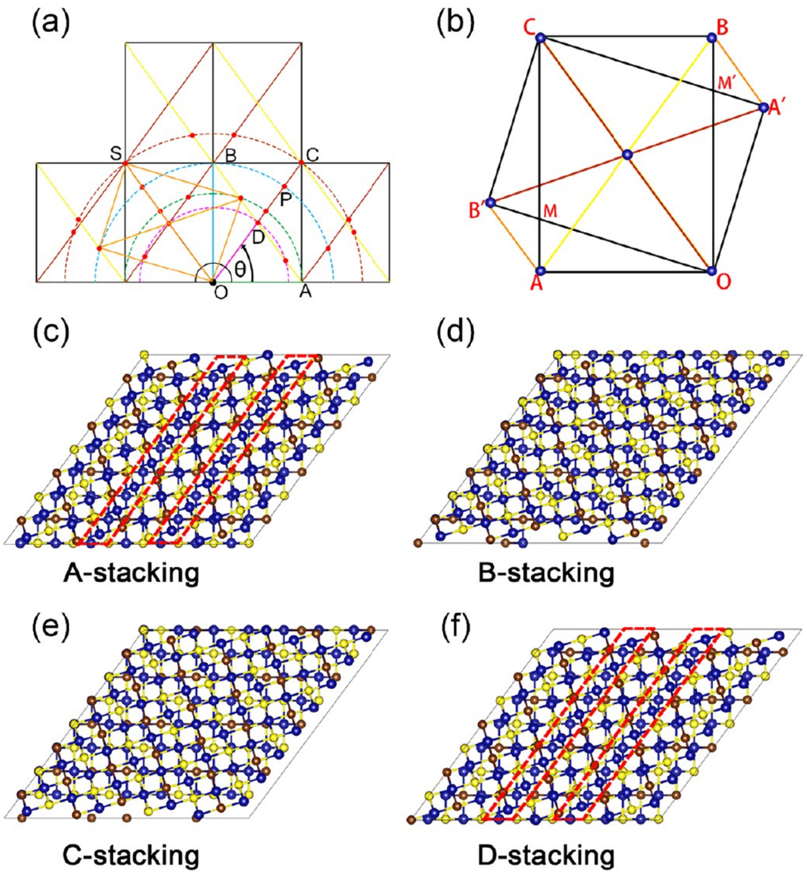

Figure 2. (a) Geometric diagram of the CrSBr twist. (b) Lattice relationship between the two layers for θ of 73°. (c−f) The structures of four stacking modes for θ of 73°.

(SOC) is considered in the calculation of the magnetic anisotropy energy (MAE). The energy convergence threshold and Hellmann−Feynman force tolerance during structural relaxation were set to 10^{-5} eV and 0.01 eV/Å, respectively. A vacuum layer of 16 Å along the **c**-axis was adopted to eliminate the spurious interlayer interaction. The plane-wave basis set cutoff energy was fixed at 400 eV. For the pristine BL CrSBr, Γ-centered Monkhorst−Pack[61] *k*-meshes of 6 × 6 × 1 and 11 × 9 × 1 were utilized for geometry optimization and energy calculation, respectively. Phonon dispersion curves were computed via the finite displacement method, implemented in the Phonopy package.[62] Postprocessing analyses, including band structure and density of the states (DOS) visualization, charge density difference (CDD), and spin charge density mapping, were conducted with the VASPKIT.[63] The AIMD simulation was performed with the aid of the DMol^3 software.[64,65] A time step of 1.0 fs and a total of 10,000 steps were set. The system is simulated at a temperature of 300 K, under the NVT ensemble with an MGGMT thermostat.

■ RESULTS AND DISCUSSION

CrSBr possesses an orthorhombic structure and belongs to the *Pmmn* space group. The optimized lattice constants for BL CrSBr along the *a* and *b* are 3.508 and 4.763 Å,[66] as shown in Figure 1a. Each Cr atom coordinates with four S atoms and two Br atoms, forming a distorted octahedron with C_{2v} group symmetry. The adjacent layers are coupled through vdW interaction, with Cr atoms exhibiting an alternating vertical displacement between upper and lower positions within the individual ML (Figure 1b, blue spheres). We constructed the twisted structure by fixing one layer and rotating the other layer, as shown in Figure 1c. CrSBr has orthorhombic lattice symmetry, so the twist periodicity is 180°. It means that the effective θ range is 0−90°, which is different from the existing twist hexagonal lattice, such as TBLG[67] and twisted BL MoS_2.[68] We constructed TBLC structures by combining two supercells obtained through enumeration of all nearly congruent supercells of ML CrSBr within a specific range of atomic counts. Then, we successfully found supercells with θ values of 17°, 25°, 37°, 48°, 60°, 73°, and 90°, respectively. The top views of twisted structures with θ of 17° and 48° are shown in Figure 1d,e, respectively. (For other twisted structures, see Figure S1 in the Supporting Information.) The θ values are observable within the lattice, demonstrating the successful construction of the TBLC supercell.

It is well-known that the interlayer stacking mode has a significant impact on the magnetic and electronic properties of 2D materials.[69] To account for the combined effects of stacking modes and θ, we calculated the TBLCs with four stacking modes at each θ. Four distinct stacking modes can be obtained by translating along the *a* and *b* axes of the CrSBr unit cell by $0, \frac{\vec{a}}{2}, \frac{\vec{b}}{2}$, and $\frac{\vec{a}+\vec{b}}{2}$, respectively. We define these as A-, B-, C-, and D-stackings, as shown in Figure S2a−d, respectively. These four stacking modes are often considered in other studies.[52,58] For the twist structure, the same approach is adopted. All A-stacking geometries at various angles are obtained by rotating the BL structure with A-stacking around the lattice vertex (i.e., the atom in the red circle in Figure S2a).

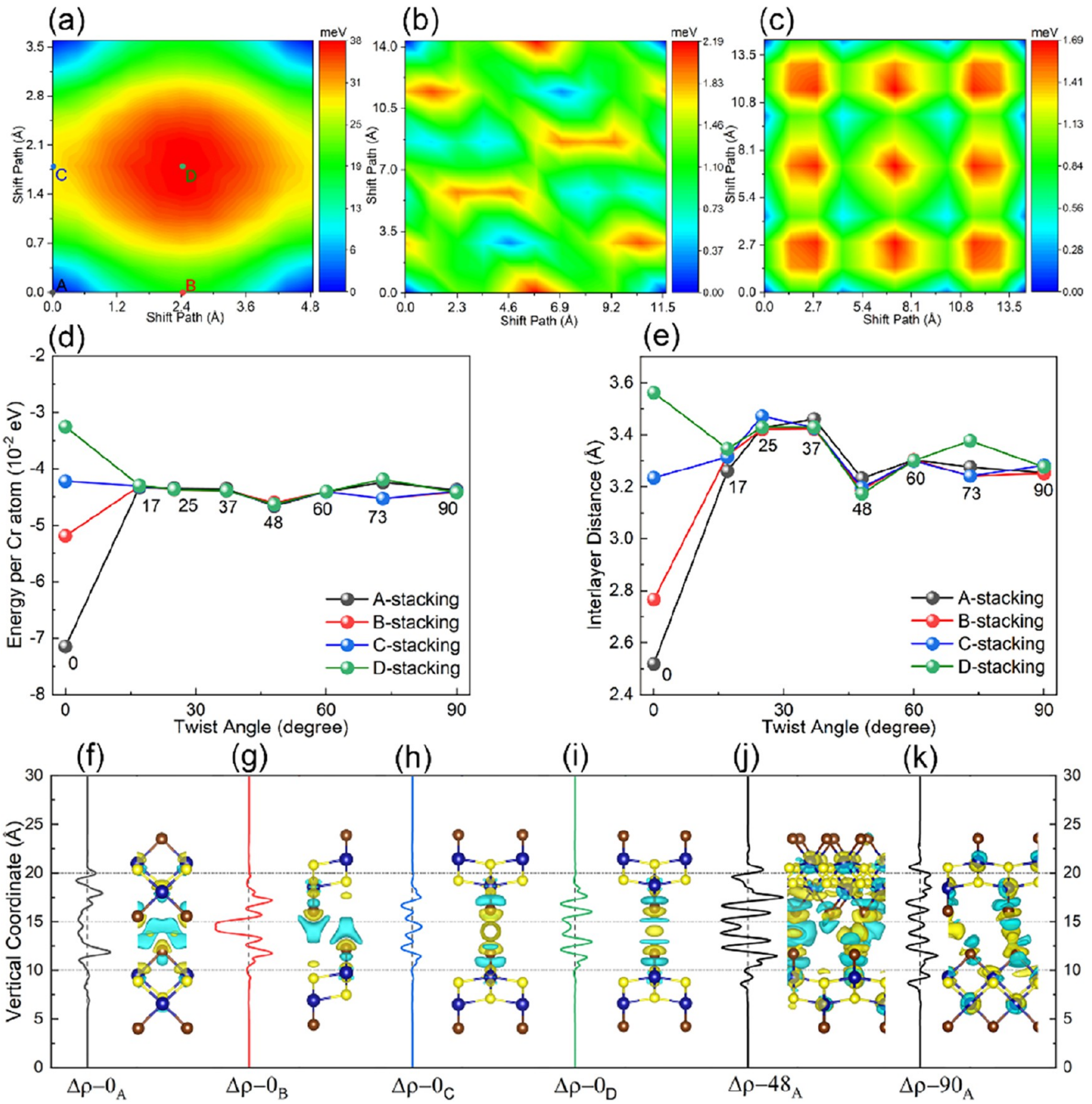

Figure 3. Energy difference with θ of (a) 0°, (b) 48°, (c) 90° as a function of lateral shift. (d) Energy per Cr atom and (e) interlayer distance for different θ and stacking modes of CrSBr. (f)−(k) Integrated CDD and CDD along the **c**-axis with θ: (f) 0°-A, (g) B, (h) C, (i) D, (j) 48°-A, and (k) 90°-A stackings. The isosurface value is 4.9×10^{-5} e/bohr^3.

And the corresponding B, C, and D stacking modes can be achieved by fixing the atoms of the lower layer and translating the atoms of the upper layer along the a and b axes of the CrSBr unit cell by $\frac{\vec{a}}{2}$, $\frac{\vec{b}}{2}$, and $\frac{\vec{a}+\vec{b}}{2}$, respectively. (For more details, see Figures S2 and S3 in the Supporting Information.)

Despite the lower symmetry of the orthorhombic lattice compared to the hexagonal lattice of graphene, which generally prevents the formation of long-range ordered moiré patterns in most twisted configurations, θ can still induce periodic stripe-like superlattice structures. Figure 2a illustrates the geometric construction principle of lattice rotation: the six rectangles represent the fixed bottom layer with lattice constants a = 3.508 Å and b = 4.763 Å, while the top layer OACB is rotated by the θ around the origin O. Each point of O, A, B, C, and D corresponds to Cr atoms. By the construction of four circular arcs centered at OA, OB, OC, and OD, the intersection points of these arcs with the diagonals of other rectangles indicate the formation of observable parallel stripes (i.e., parallel lines within the lattice), as highlighted by the red dots in Figure 2a. Adopting the AOB coordinate system, the coordinates of the rotated points are derived as follows

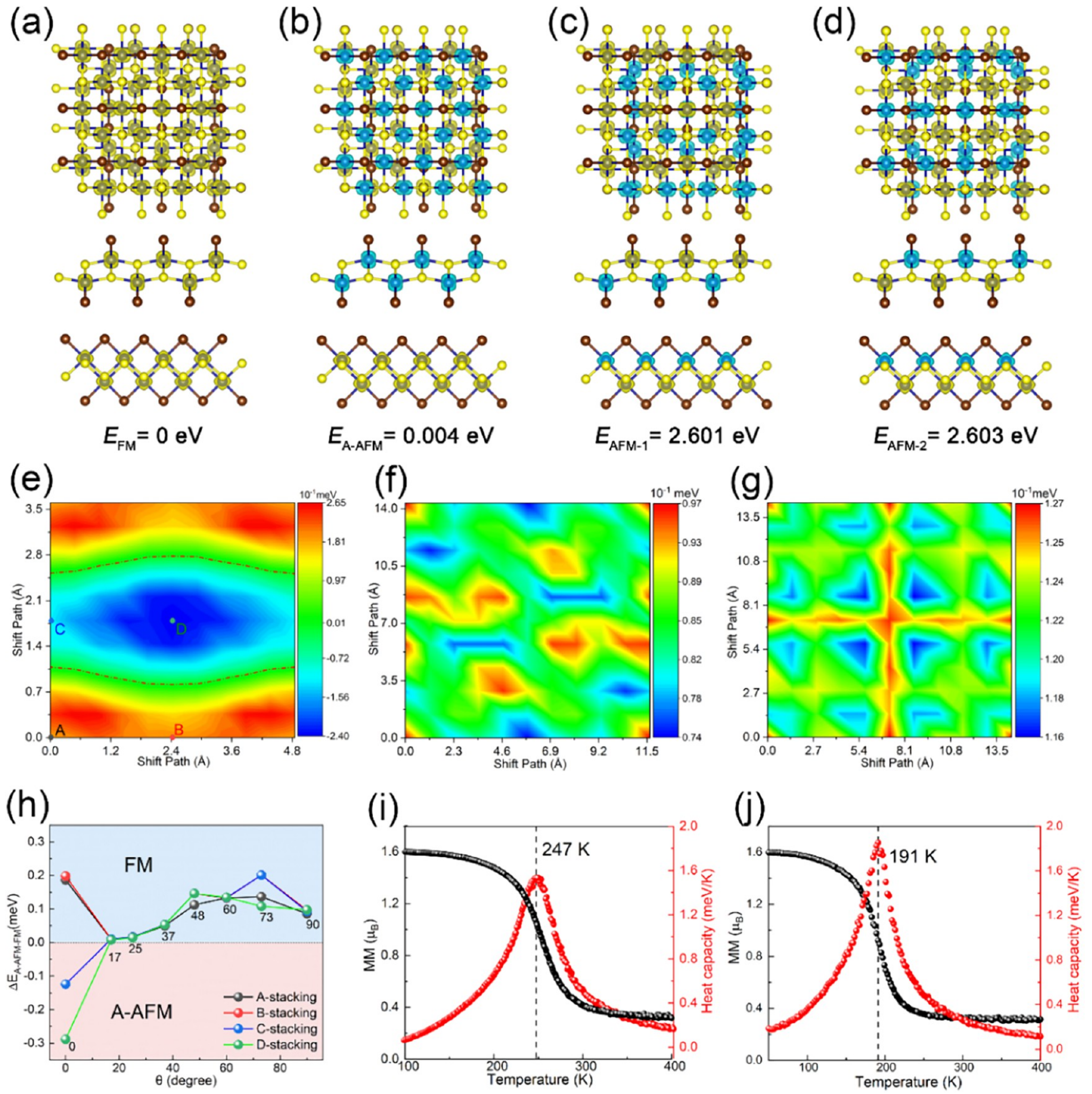

Figure 4. (a−d) Four magnetic orders with θ of 90° A-stacking structure. The energy difference between FM and A-AFM orders with θ of (e) 0°, (f) 48°, and (g) 90° as a function of lateral shift. (h) The energy difference between FM and A-AFM orders for different θ and stacking modes of CrSBr. MM and heat capacity as a function of temperature in T_c simulation for θ of (i) 48° and (j) 90°, respectively. The isosurface value is 0.061 e/bohr^3.

$$A'\colon\ (a\cos\alpha,\ a\sin\alpha)$$

$$B'\colon\ (-b\sin\alpha,\ b\cos\alpha)$$

$$C'\colon\ (a\cos\alpha-b\sin\alpha,\ \ a\sin\alpha+b\cos\alpha)$$

$$D'\colon\ \left(\frac{a\cos\alpha-b\sin\alpha}{2},\ \frac{a\sin\alpha+b\cos\alpha}{2}\right)$$

Take point P as an example; by solving the intersection condition of the rotated lattice with the diagonal line $y = (b/a)\,x$, $\theta = 36°$ is obtained. The structure with θ of 36° is shown in Figure S4, where it can be seen that there are certain stripes. More intriguingly, among these special θ, a particularly unique configuration occurs at $\theta = 73°$. In this case, four points A–D of the rotated rectangle simultaneously lie on the diagonals of the bottom-layer unit cell, resulting in a structure, shown in Figure 2b. It can be proven that triangles $\Delta MB'C$ and ΔMAO are congruent and $AB'\|OC\|A'B$. This geometric symmetry indicates the alignment of Cr atoms along the diagonals with the remaining four Cr atoms also parallel to the diagonal atoms, leading to the observation of distinct stripe patterns, as illustrated in Figure 2c−f, respectively. These patterns remain robust against the changes in stacking modes. In certain specific stacking modes, the alignment of Cr atoms from both layers into straight lines becomes even more pronounced, which can be seen in Figure 2c,f, respectively. The unique 73° twisted structure characteristics endow it with distinct properties compared to other θ, which we will discuss in the following sections.

We systematically investigated the θ dependence of interlayer coupling through a comparative energy analysis. Figure 3a−c maps the energy landscapes for distinct stacking modes with θ values of 0°, 48°, and 90°, respectively. In the pristine BL, A-stacking emerges as the reference state with minimal energy (set as reference 0 meV/Cr). The energy progression follows: $\Delta E_{\text{A-stacking}}$ (0) < $\Delta E_{\text{B-stacking}}$ (+12 meV/Cr) < $\Delta E_{\text{C-stacking}}$ (+23 meV/Cr) < $\Delta E_{\text{D-stacking}}$ (+38 meV/Cr), where the stacking energy difference ΔE_{stack} is defined as $\Delta E_{\text{stack}} = E_{\text{stack}} - E_{\text{A-stacking}}$. It can be concluded that there is axial translation anisotropy: translation along the shorter **a**-axis induces faster energy escalation than that along the **b**-axis. Due to the variation in lattice size for different θ, all energies mentioned in this work are normalized by the number of Cr atoms to make consistent comparisons. This anisotropic behavior correlates with the orthorhombic lattice symmetry, evidenced by mirror-symmetric energy contours along the B−D and C−D directions (Figure 3a). However, θ disrupts this symmetry, generating complex moiré-induced potential modulation. The energy landscapes with θ values of 48° and 90° exhibit significantly increased complexity compared to the pristine BL. However, they retain periodic symmetry and central inversion symmetry (Figure 3b,c), originating from multiple equivalent interlayer sliding pathways across the scanning plane. Notably, the energy difference between different stacking configurations is 2.19 meV (48°) and 1.69 meV (90°), which are much smaller than pristine BL (38 meV). This dramatic narrowing of energy dispersion demonstrates that the twist suppresses the dependence of interlayer coupling on the stacking modes, as the moiré superlattice periodicity breaks the regular coupling of the original lattice with larger θ.

The energy and interlayer distance evolution across θ are shown in Figure 3d,e, respectively. (For the definition of interlayer distance, please refer to the Supporting Information, Figure S5.) It can be observed that for the pristine BL, interlayer sliding has a significant impact on both energy and interlayer distance, and the energy ordering is also reflected in the interlayer distance. But the difference of interlayer distance between different stacking modes is confined to 0.059 and 0.031 Å for the θ of 48° and 90°, which are much smaller than 1.044 Å (0°), as shown in Figure 3e. When θ is introduced, the influence of interlayer sliding is greatly reduced for both energy and interlayer distance. This is attributed to θ, which complicates interlayer coupling. During the transition between different stacking modes, some couplings strengthen while others weaken, resulting in an overall cancellation of differences. Interestingly, the impact of different stacking modes on interlayer interaction with θ of 73° is more pronounced, compared to other angles. Its origins are that the structure is unique, with Cr atoms arranged in a more regular pattern within the unit cell, leading to more orderly interlayer coupling. When the structure translates from Stacking-B to Stacking-D, all Cr−Cr interatomic distances systematically decrease, indicating a coordinated enhancement of exchange coupling throughout the system, as shown in Figure 2d,f. This stands in marked contrast to other θ, where interlayer sliding simultaneously increases some Cr−Cr distances while decreasing others, resulting in a net cancellation effect that diminishes stacking-dependent responses.

As a result, the response to interlayer sliding is also more pronounced. The energies of CrSBr with different θ values are relatively similar, with the overall distribution ranging from −0.047 to −0.042 eV/Cr. However, θ has a more pronounced effect on the interlayer distance, with the overall distribution spanning from 3.17 to 3.47 Å.

Among them, 48° exhibits the lowest energy and interlayer distance, indicating the strongest interlayer interaction. To further understand the difference in interaction, we also plotted the planar average charge difference and CDD in Figure 3f−k, respectively. It can be observed that the curves and CDDs corresponding to the four stacking modes of pristine BL CrSBr exhibit significant variation. When the twist is introduced, the CDD becomes more complex, with charge transfer between Br atoms in different positions varying significantly and the charge integration curves showing more oscillations.

Magnetic Properties. To investigate the magnetic properties, we tested different magnetic orders for each θ. The magnetic moments (MM) of CrSBr are primarily localized in Cr atoms, with each Cr atom having 3.1 μ_B MM, regardless of θ. First, the magnetic order of the pristine BL CrSBr was investigated. Stacking-dependent magnetic orders emerge: A and B stacking modes tend to FM order, while C and D stacking modes favor A-type antiferromagnetic (A-AFM) order (Figure S6 and Table S3). It indicates that the magnetic order of the pristine BL CrSBr is strongly correlated with the stacking modes. θ fundamentally alters this paradigm by introducing the moiré magnetism.

Figure 4a−d reveals the characteristics of magnetic orders with an θ of 90°. Among them, FM order indicates that all Cr atoms exhibit FM coupling to each other, as shown in Figure 4a. A-AFM order denotes that Cr atoms within each layer maintain FM coupling, while interlayer Cr atoms display AFM coupling (Figure 4b). AFM-1 and AFM-2 orders represent AFM coupling between Cr atoms at different heights within the CrSBr layers. On this manner, the interlayer neighboring Cr atoms in the AFM-1 order exhibit FM coupling (Figure 4c), while those in the AFM-2 order exhibit AFM coupling (Figure 4d). In addition, we also considered eight other magnetic orders, as shown in Figure S7. Among these orders, the FM order exhibits the lowest energy. Besides, we observed that disrupting FM coupling within CrSBr layers leads to a significant increase in energy (at least 0.4 eV). It demonstrates that twist could not obviously interfere with the strong intralayer FM coupling in CrSBr.

To elucidate the stacking-dependent magnetic coupling in CrSBr, we systematically mapped the energy difference landscapes of FM and A-AFM orders ($\Delta E = E_{\text{A-AFM}} - E_{\text{FM}}$) as functions of in-plane sliding coordinates for θ values of 0°, 48°, and 90°, as shown in Figure 4e−g, respectively. The pristine BL exhibits stacking-controlled magnetic phase separation (Figure 4e). The primitive cell is divided into two distinct regions: A/B-stacking domains with dominant FM coupling ($\Delta E > 0$) and C/D-stacking domains favoring AFM ordering ($\Delta E < 0$), separated by a sharp phase boundary (red dashed line). Twist dramatically suppresses this stacking−magnetism correlation. For the twisted CrSBr at θ of 48° and 90°, all regions exhibit positive ΔE (Figure 4f,g), indicating robust FM order, independent of the stacking modes. The fluctuation of ΔE ranges from 0.023 to 0.011 meV for θ = 48°

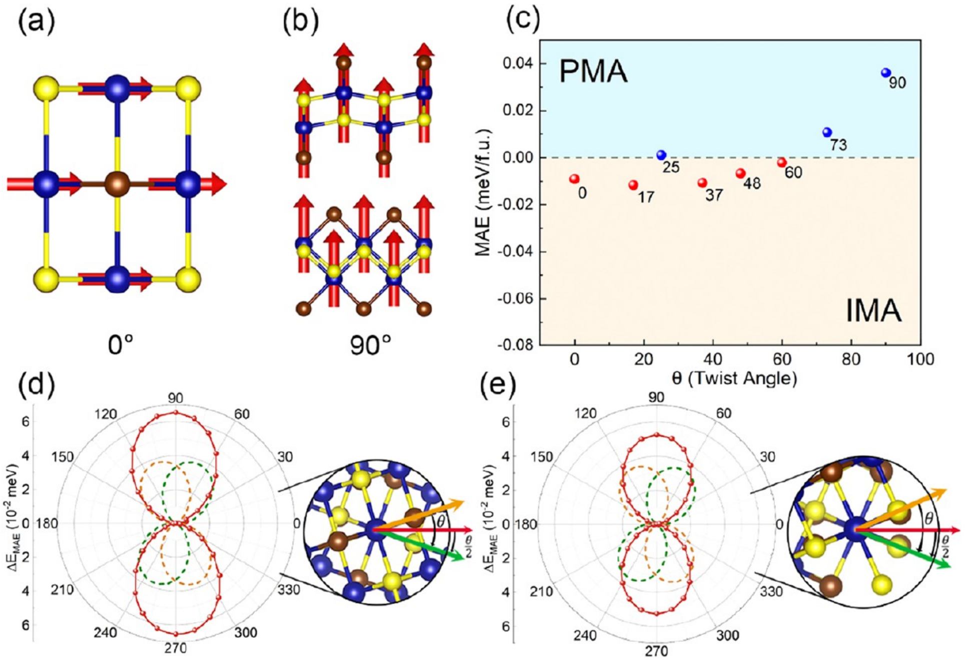

Figure 5. EA along the directions of (a) 0° and (b) 90°. (c) MAE as a function of *θ*. (d, e) Angle dependence of MAE of *θ* of (d) 37° and (e) 48° with the spin orientation along the *xoy* plane. (The red lines represent twisted BL, while the yellow and green lines represent the upper and lower CrSBr MLs, respectively.).

and 90°, respectively, compared to 0.505 meV (0°). Similar to Figure 3a−c, the energy landscape diagrams still have central symmetry.

For each stacking mode with other *θ*, we also calculated the energies of Δ*E*, as shown in Figure 4h. It is evident that when *θ* exists, regardless of the stacking modes, the system exhibits FM order. Moreover, the energy difference between the different stacking modes is significantly reduced. This dramatic suppression originates from twist-induced complexity in interlayer exchange coupling: as layers slide, some enhanced Cr−Cr interaction is counterbalanced by weakened coupling in others, resulting in near-complete cancellation of the stacking-dependent energy difference. However, two notable exceptions emerge at the specific *θ*. The *θ* of 48° displays Δ*E* fluctuation of 0.034 meV, which is due to the smaller moiré superlattice, where the interlayer sliding has a more pronounced impact on the interlayer coupling. The *θ* of 73° exhibits revived stacking dependence (0.093 meV fluctuation) due to its unique supercell. The regular alignment of Cr sublattices in this configuration creates geometrically ordered coupling channels, enabling a systematic response to layer sliding.

A high T_c is a key indicator of an FM material's ability to maintain magnetic order at an elevated temperature. We used the Monte Carlo simulation method based on the Heisenberg model to calculate the magnetic exchange constants. We consider three intralayer magnetic exchange interactions (J_1, J_2, J_3), where J_1, J_2, and J_3 represent the nearest, the second-nearest, and the third-nearest intralayer neighbors, respectively. Thus, its spin Hamiltonian can be expressed as follows

$$H = -J_1 \sum_{ij} \vec{S}_i \vec{S}_j - J_2 \sum_{ij} \vec{S}_i \vec{S}_j - J_3 \sum_{ij} \vec{S}_i \vec{S}_j - K_u \sum_{i} (S_i)^2 \qquad (1)$$

where $\vec{S}$ and K_u represent the spin operator and anisotropy constant, respectively. For $\theta = 48°$, we employed four distinct magnetic orders in our calculation: FM, AFM-1, FiM-1, FiM-2, as shown in Figure S8. Our calculation yields the following magnetic exchange parameters: J_1, J_2, and J_3 are 6.51, 5.18, and −0.07 meV, respectively. For *θ* of 90°, we consider FM, FiM-1, FiM-2, and FiM-3 orders to calculate magnetic exchange constants, as shown in Figure S8. The J_1, J_2, and J_3 are 4.86, 5.30, and −1.68 meV, which are considered in calculating T_c. The results show that T_c equals 247 K for 48° (Figure 4i), 191 K for 90° (Figure 4j). It demonstrates that *θ* modulates T_c by altering the strength of the intralayer exchange interaction. For the pristine BL CrSBr, the Néel temperature (T_N) of approximately 140 K was experimentally determined using second-harmonic generation (SHG) techniques.[70] It can be concluded that *θ* could enhance the stability of the long-range FM order.

Magnetic Anisotropy Properties. Magnetic anisotropy refers to the direction dependence of the MM in a material. The MAE represents the energy difference between the MM aligned along the EA and hard axis. Higher MAE corresponds to the enhanced stability of the magnetic orientation against external perturbation. For each TBLC, we performed a 360° in-plane (*xoy* plane) angular scan of the magnetic orientation to determine the EA direction. Subsequently, the out-of-plane $E_{[001]}$ was compared to the in-plane EA direction to determine whether the system exhibited PMA or in-plane magnetic anisotropy (IMA).

The pristine BL exhibits robust IMA with the EA locked along the crystallographic **a**-axis (Figure 5a). Remarkably, the twist induces the EA switch: the *θ* of 90° transitions to PMA with EA oriented perpendicular to the plane, as shown in Figure 5b. Figure 5c reveals a nonmonotonic MAE evolution with *θ*, where the magnetic anisotropy alternates between IMA and PMA multiple times as *θ* increases. Among them, the structures with the *θ* of 0°, 17°, 37°, 48°, and 60° present IMA, while 25°, 73°, and 90° present PMA. As the *θ* increases, the overall trend is that the value of MAE gradually rises. The strong *θ*-dependence of magnetic anisotropy establishes *θ* as a

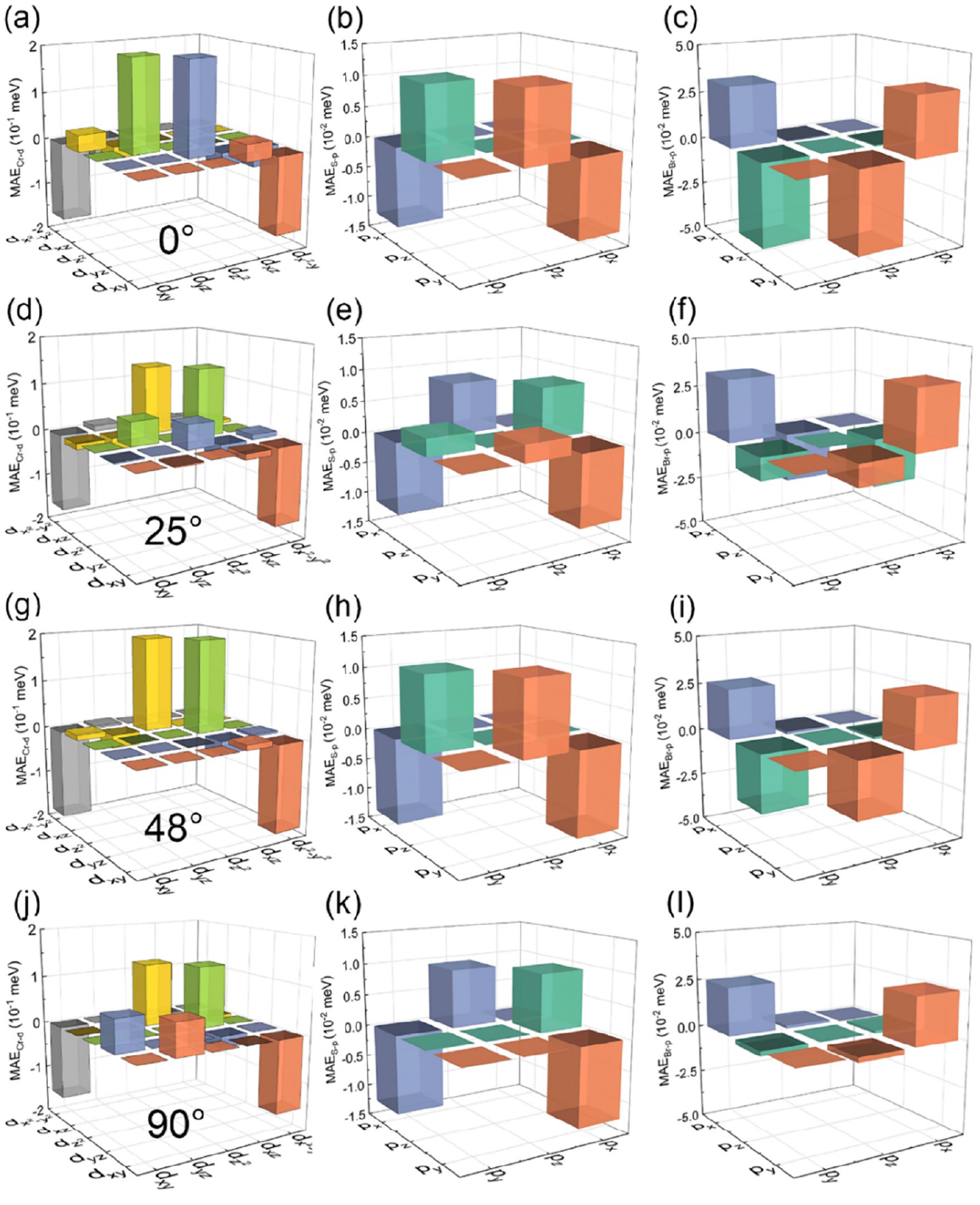

Figure 6. Orbital-resolved MAE of TBLCs with θ of (a–c) 0°, (d–f) 25°, (g–i) 48°, and (j–l) 90°. Orbital-resolved MAE: (a) 0°-Cr-d, (b) 0°-S-p, (c) 0°-Br-p, (d) 25°-Cr-d, (e) 25°-S-p, (f) 25°-Br-p, (g) 48°-Cr-d, (h) 48°-S-p, (i) 48°-Br-p, (j) 90°-Cr-d, (k) 90°-S-p, and (l) 90°-Br-p.

powerful tuning parameter for magnetic anisotropy engineering.

Intriguingly, the in-plane EA direction in TBLCs (e.g., 37° and 48°, Figure 5d,e) aligns precisely with the angular bisector of each layer's original EA. It can be observed that as θ

Table 1. Orbital-Resolved MAE of TBLC for Different θ

atom orbital	MAE for different θ (μeV)							
	0	17	25	37	48	60	73	90
Cr-d	1.75	−2.33	5.45	−0.53	−1.83	−7.77	−8.97	12.21
S-p	−1.25	−1.41	−0.66	−3.35	−1.77	−2.32	−1.19	−3.25
Br-p	−12.0	−8.73	−4.49	−7.93	−4.50	6.21	18.27	24.15

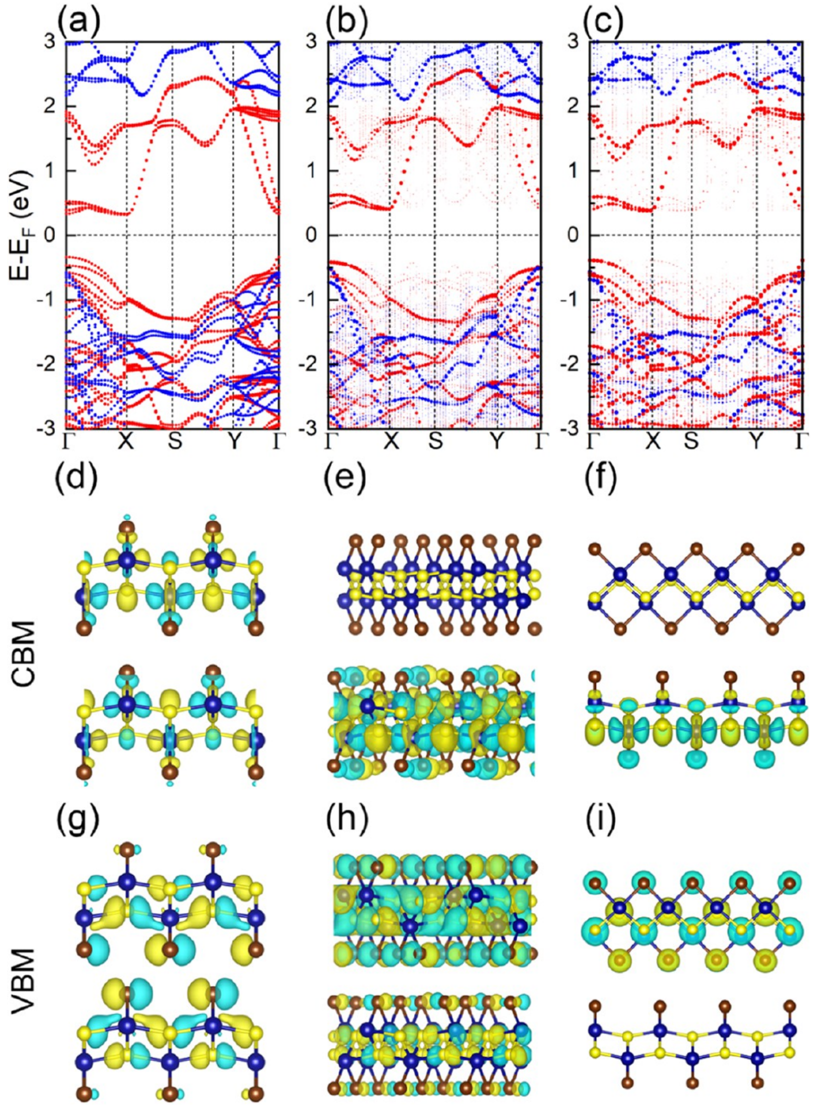

Figure 7. Band structure of TBLCs with θ values of (a) 0°, (b) 48°, and (c) 90°. The CBM wave function with θ of (d) 0°, (e) 48°, and (f) 90°. The VBM wave function with θ of (g) 0°, (h) 48°, and (i) 90°. The blue and yellow represent the phase of the wave function. The isosurface value is 7.5×10^{-9} e/bohr^3.

increases, the in-plane magnetic axis energy difference (ΔE_{MAE}) decreases. The radius of the dumbbell curve becomes smaller. This proves that the MAE of TBLC is a superposition of contributions from the upper and lower layers. As θ increases, the contribution of each CrSBr layer to the overall EA direction diminishes, resulting in a smaller energy difference. However, θ has a relatively minor impact on the energy of TBLCs along the vertical direction of the magnetic axis. As the θ gradually increases, the energy within the plane gradually increases, leading to the transition from IMA to PMA.

We further constructed a three-layer CrSBr structure with an θ of 48°. In-plane EA reveals alignment along 16° ($\frac{\theta}{3} = 16°$) direction, indicated by the red arrow in Figure S9. This phenomenon appears as the original EA of the top and bottom CrSBr layers maintains identical orientation (0° direction), while the middle layer's axis shifts due to the twist.

When the magnetic anisotropy vectors of the three layers undergo superposition, the collinear contribution from the outer layers dominates, driving the resultant EA close to the outer layer direction. This observation further verifies our conclusion: the direction of in-plane EA is determined by the

https://doi.org/10.1021/acs.jpcc.5c04752
J. Phys. Chem. C XXXX, XXX, XXX−XXX

vector superposition of magnetic anisotropy from individual CrSBr ML.

Atom-Orbital-Resolved MAE. To explain the origin of the MAE transition, the atom-orbital-resolved MAE is calculated, employing tight-binding and second-order perturbation theory.[71] The MAE of each atom (MAE_i) can be assessed by applying the canonical formulation equation:

$$\mathrm{MAE}_i = \left[\int E_{\mathrm{f}}(E - E_{\mathrm{F}})[n_i^{[xy0]}(E) - n_i^{[001]}(E)]\right] \quad (2)$$

where MAE_i represents the ith atom's MAE. $n_i^{[xy0]}(E)$ indicates the DOS of the ith atom with the magnetic axis along the in-plane direction with the lowest energy. $n_i^{[001]}(E)$ denotes the DOS of the ith atom with the magnetic axis along the [001] direction, which is perpendicular to the plane. Moreover, the total MAE can be obtained by summing the contribution from each atom (MAE_i). Within the framework of second-order perturbation theory,[72] the MAE can be derived from the following terms

$$\Delta E^{--} = E_x^{--} - E_z^{--} = \xi^2 \sum_{o^+,u^-} (|<o^-|L_z|u^->|^2 - |<o^-|L_x|u^->|^2)/(E_u^- - E_o^-) \quad (3)$$

$$\Delta E^{-+} = E_x^{+-} - E_z^{+-} = \xi^2 \sum_{o^+,u^-} (|<o^+|L_z|u^->|^2 - |<o^+|L_x|u^->|^2)/(E_u^- - E_o^-) \quad (4)$$

where +and −represent spin-α and spin-β electrons, respectively. ξ, L_x, and L_z are SOC constants, associated with the angular momentum operators along the [xy0] and [001] directions, respectively. u and o values represent unoccupied and occupied states, and E_o and E_u are the energies of occupied and unoccupied states, respectively. In addition to this, the matrix element differences $|<o^-|L_z|u^->|^2 - |<o^-|L_x|u^->|^2$ and $|<o^+|L_z|u^->|^2 - |<o^+|L_x|u^->|^2$ for d and p orbitals are calculated, shown in Tables S2 and S3, respectively.

To further explain the variation of MCA, the atom-orbital-resolved MAE is calculated, as shown in Figure 6. The contribution of Cr, S, and Br atoms to MAE is shown for θ of 0°, 25°, 48°, and 90° from top to bottom. And the other θ of 17°, 37°, 60°, and 73° are shown in Figure S10. For the pristine BL CrSBr, the MAE contributions from Cr-d orbitals, the S-p orbitals, and Br-p orbitals are 1.75, −1.25, and −12 μeV, respectively. It can be observed that the contribution of Br atom to the MAE is significantly larger than that of the Cr and S atoms. Additionally, the interaction between $\mathrm{d}_{x^2-y^2}$ and d_{xy} orbitals and the interaction between d_{z^2} and d_{yz} orbitals of Cr atoms are the strongest, with the values of −166 and 197 μeV, respectively. For S atoms, the strongest interaction occurs between p_x and p_y orbitals, and between p_y and p_z orbitals, with the values of −12.7 and 11.3 μeV, respectively. For Br atoms, the stronger interaction also occurs between p_x and p_y orbitals, and between p_y and p_z orbitals, with the values of 31.9 and −43.6 μeV, respectively.

When θ is present, it can be observed that the primary contribution to the MAE for each element remains unchanged. The lattice vectors of the unit cell of CrSBr and the constructed supercell form a certain angle, which could cause the exchange of orbitals in the x and y directions. We consider this to be the same type of interaction. However, the θ significantly modulates both direction and magnitude of projected MAE, as shown in Table 1. It can be observed that θ has a more pronounced effect on the Cr-d and Br-p orbitals, compared to the S-p orbitals. For θ values of 60°, 73°, and 90°, the MAE contribution from the Br-p orbital is 6.21, 18.27, and 24.15 μeV, respectively. This indicates that as the θ approaches 90°, the Br-p orbital gradually contributes more to the out-of-plane MAE, resulting in the EA of TBLC stabilizing predominantly in the vertical direction.

Our analysis of wave function evolution and band structure modulation in TBLC reveals θ-dependent electronic state reorganization. The electronic structures of CrSBr with different θ values have been systematically investigated. Due to the distinct supercell lattice structures induced by twist, the superlattice bands were projected onto the original Brillouin zone of the pristine BL CrSBr, using reciprocal space transformation matrices (see Figure S11 for matrix details and schematic).[70,73] To eliminate the influence of stacking modes on the electronic structure, all band structures and wave functions have been calculated based on the A-stacking at each θ.

In Figure 7a−c, the unfolded band structures reveal three θ-dependent features: Twist can induce spin polarization in the CrSBr BL. All TBLCs preserve half-semiconductor (HSC) characteristics, with both the conduction band minimum (CBM) and the valence band maximum (VBM) dominated by the same spin channel. The band gaps are 0.661 eV (0°), 0.842 eV (48°), and 0.764 eV (90°), displaying a nonmonotonic angular dependence. While the VBM is still located at the Γ point across these angles, the CBM undergoes a critical position transition, residing at the X point (X = 0,5, 0,0) for the θ of 0° and 48°, but it shifts to the Γ point at 90°. It indicates that θ drives the transition from indirect to direct semiconductors, which stems from the reconstruction of interlayer orbital hybridization between Cr and Br atoms. Such an effect highlights the potential of twist engineering for tailoring optoelectronic properties in van der Waals magnets. We also investigate the DOS at various θ, as shown in Figure S12. All DOS confirm that TBLC retains HSC. Interestingly, the elemental contribution to DOS near the Fermi level varies significantly with θ. Cr atoms dominate DOS near the Fermi level, at θ values of 0°, 17°, 25°, 37°, 48°, and 90°. In contrast, S and Br atoms become the primary contributors at 60° and 73°. This observation suggests that θ modulates the orbital interaction among these elements. (See Supporting Information for details.)

In the pristine BL CrSBr, the CBM primarily derives from the contribution of Cr atoms and S atoms, while the VBM is mainly composed of S atoms and interlayer Br atoms. Crucially, the wave functions of both CBM and VBM are completely delocalized across the upper and lower layers. We have calculated the wave functions of CBM and VBM with θ of 0°, 48°, and 90°, as shown in Figure 7d−i. For the pristine BL CrSBr, the CBM is mainly contributed by Cr and S atoms, while the VBM is primarily composed of S atoms and the inner Br atoms of both layers. The wave function of both CBM and VBM is delocalized across the two layers (Figure 7d,g). For 48°, the CBM wave function becomes localized on the bottom CrSBr layer, whereas the VBM wave function is predominantly concentrated in the upper layer with a small portion extending to the lower layer (Figure 7e,h). In the case of 90°, the CBM wave function is completely localized on the lower layer, while the VBM wave function is entirely confined to the upper layer, achieving spatial separation of electron and hole (Figure 7f,i).

The same phenomenon also occurs in the twisted black phosphorus homostructures[74] and MoS$_2$/WS$_2$ heterobilayers.[75] This separation of carriers can effectively prolong the exciton lifetime and is suitable for hot carrier extraction in photovoltaic devices.

To further explain this phenomenon, we project the original band structures onto the upper and lower layers, as shown in Figure S13. For a pristine BL CrSBr, the projected bands of the two layers are nearly identical. However, when θ is introduced, the band exhibits a significant difference, which corresponds to the variation in the wave function. We attribute this to the suppression of vertical hybridization between the originally aligned Cr-d$_{z^2}$ and Br-p$_z$ orbitals by θ, which cuts off the interlayer extension path of the wave function.

Phonon Spectrum and AIMD Simulation. To confirm the dynamic stability of the twisted structure, comprehensive phonon dispersion and phonon density of states (PHDOS) analyses have been performed, as presented in Figure 8. (The k-point paths for each structure are shown in Figure S14.) The absence of imaginary frequency in the phonon spectra for θ values of 0°, 48°, and 90° confirms the thermodynamic stability. For the pristine BL CrSBr, the optical branches are well separated at the Γ point, while some branches become degenerate, which is related to the symmetry of the CrSBr lattice, at the X and Y points. The maximum phonon frequencies for θ of 0°, 48°, and 90° are 10.87, 10.93, and 10.72 THz, respectively, indicating that θ could modulate lattice vibrational frequencies. PHDOS can be divided into three parts. In the low-frequency regime (0−4 THz), the phonon modes are predominantly contributed by the heavier Br atoms, corresponding to acoustic vibrations. The mid-frequency range (4−8 THz) exhibits comparable contribution from all constituent elements. At higher frequencies (8−11 THz), lighter S and Cr atoms dominate the vibrational spectrum, characteristic of optical phonon modes. The three PHDOS display prominent peaks at 1.7, 3, 6, 9, and 10.5 THz, indicative of localized vibrational modes associated with the flat region in the phonon dispersion curves.

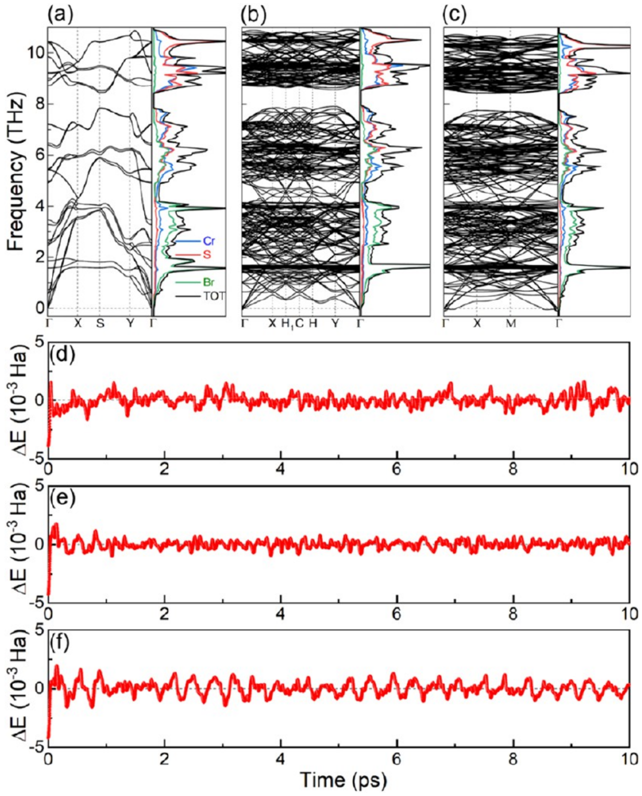

Figure 8. Phonon band and PHDOS of TBLC with the θ of (a) 0°, (b) 48°, and (c) 90°. The blue, red, green, and black lines represent Cr, S, Br, and total PHDOS, respectively. Function of energies with θ of (d) 0°, (e) 48°, (f) 90° in the simulated temperature of 300 K.

To demonstrate the thermodynamic stability of TBLC, an AIMD simulation was performed at 300 K. Figure 8d−f shows the energy fluctuation around −845.319, −845.323, and −845.324 Ha for the θ of 0°, 48°, and 90°, respectively. The average energy fluctuation per atom with θ of 0°, 48°, and 90° at 300 K are 0.0029, 0.0017, and 0.0027 Ha, respectively. Random snapshots of the geometry during the simulation also prove the structural integrity, as shown in Figure S15. In addition, the AIMD simulations with θ values of 17°, 25°, 37°, and 73° are also performed, as shown in Figure S16. All simulated results demonstrate the excellent dynamic stability of the TBLC.

■ CONCLUSIONS

In this work, we systematically investigated the twist engineering of magnetic properties and electronic structures in CrSBr BL through first-principles calculation. The θ fundamentally modulates interlayer interaction, magnetic order, and magnetic anisotropy via moiré superlattice engineering. Three critical phenomena emerge: (1) θ stabilizes FM order in CrSBr BL, independent of stacking modes, which contrasts strikingly with the stacking-dependent magnetism in pristine BL. Notably, the θ of 73° exhibits unique stripe-like moiré patterns that revive stacking sensitivity through a geometrically ordered coupling channel. (2) Nonmonotonic magnetic anisotropy transitions are observed, which successively alternate between IMA and PMA as θ increases. (3) Orbital-resolved analysis identifies Br-p orbital as the dominant contributor to PMA, with their contribution amplifying by 200% at θ of 90° compared to 0°.

The nonvolatile memory elements can be effectively designed by utilizing the θ-controlled EA switching between IMA and PMA. This unique switching behavior enables multistate memory operation through precise control of magnetization orientations. Furthermore, the discovery of twist-dependent bandgap modulation and layer-separated charge carrier localization suggests a potential application in twist-tunable optoelectronic devices. Finally, the phonon spectra and AIMD simulations collectively validate the experimental realizabilities of TBLCs. Our work establishes CrSBr as a prototypical platform for moiré magnetism studies in orthorhombic vdW magnets, expanding the material base for twistronics beyond the conventional hexagonal system.

■ ASSOCIATED CONTENT

Data Availability Statement

The data that support the findings of this study are available from the corresponding author upon reasonable request.

SI Supporting Information

The Supporting Information is available free of charge at https://pubs.acs.org/doi/10.1021/acs.jpcc.5c04752.

Remaining calculation parameter of AIMD simulation, the principle of the twisted supercell lattice of CrSBr, the structures of each θ, different stacking modes of CrSBr, the translation schematic diagram, the magnetic orders of pristine BL, different magnetic orders with θ of 90°, magnetic orders for calculating magnetic exchange constants, in-plane magnetic MAE schematic diagram of the θ of 48° trilayer structure, orbital-resolved MAE, the transformation relationship between supercells and primitive cell, DOS and band structures, phonon spectrum and AIMD simulation, and the coordinates of the high symmetry points (PDF)

■ AUTHOR INFORMATION

Corresponding Author

Zhaoyong Guan − *Key Laboratory of Colloid and Interface Chemistry, Ministry of Education, School of Chemistry and Chemical Engineering, Shandong University, Jinan, Shandong 250100, P. R. China; School of Chemistry and Chemical Engineering, Shandong University, Jinan, Shandong 250100, P. R. China;* orcid.org/0000-0002-6847-5809; Email: zyguan@sdu.edu.cn

Authors

Fangyu Zhang − *Key Laboratory of Colloid and Interface Chemistry, Ministry of Education, School of Chemistry and Chemical Engineering, Shandong University, Jinan, Shandong 250100, P. R. China; School of Chemistry and Chemical Engineering, Shandong University, Jinan, Shandong 250100, P. R. China*

Zihao Xu − *School of Physics, Shandong University, Jinan, Shandong 250100, P. R. China*

Diancong Qi − *Key Laboratory of Colloid and Interface Chemistry, Ministry of Education, School of Chemistry and Chemical Engineering, Shandong University, Jinan, Shandong 250100, P. R. China; School of Chemistry and Chemical Engineering, Shandong University, Jinan, Shandong 250100, P. R. China*

Weiyi Wang − *State Key Laboratory of Precision and Intelligent Chemistry & Hefei National Research Center for Physical Sciences at the Microscale, University of Science and Technology of China, Hefei, Anhui 230026, P. R. China;* orcid.org/0000-0001-6981-2611

Xingxing Li − *State Key Laboratory of Precision and Intelligent Chemistry & Hefei National Research Center for Physical Sciences at the Microscale, University of Science and Technology of China, Hefei, Anhui 230026, P. R. China;* orcid.org/0000-0001-7820-0772

Ya Su − *School of Electrical Engineering, Shandong University, Jinan, Shandong 250100, P. R. China*

Wujun Shi − *Center for Transformative Science, ShanghaiTech University, Shanghai 201210, P. R. China*

Complete contact information is available at:
https://pubs.acs.org/10.1021/acs.jpcc.5c04752

Notes

The authors declare no competing financial interest.

■ ACKNOWLEDGMENTS

The authors thank Prof. Wenhui Duan for the discussion of evaluation of T_c. This work was supported by the financial support from the Natural Science Foundation of China (Grant No. 11904203) and the Natural Science Foundation of Shandong Province (ZR2023MA019). The scientific calculation in this paper has been performed on the HPC Cloud Platform of Shandong University, HPC Platform for Theoretical and Computational Chemistry of the School of Chemistry and Chemical Engineering of Shandong University. The authors are grateful to the Beijing Super Cloud Computing Center (Beijing Beilong Super Cloud Computing Co., Ltd) and Hefei Advanced Computing Center.

■ REFERENCES

(1) Bistritzer, R.; MacDonald, A. H. 2D Mater bands in twisted double-layer graphene. *Proc. Natl. Acad. Sci. U.S.A.* **2011**, *108* (30), 12233−12237.

(2) Cao, Y.; Fatemi, V.; Fang, S.; Watanabe, K.; Taniguchi, T.; Kaxiras, E.; Jarillo-Herrero, P. Unconventional superconductivity in magic-angle graphene superlattices. *Nature* **2018**, *556* (7699), 43−50.

(3) Li, G.; Luican, A.; dos Santos, J. M. B. L.; Neto, A. H. C.; Reina, A.; Kong, J.; Andrei, E. Y. Observation of Van Hove singularities in twisted graphene layers. *Nat. Phys.* **2010**, *6* (2), 109−113.

(4) Cao, Y.; Fatemi, V.; Demir, A.; Fang, S.; Tomarken, S. L.; Luo, J. Y.; Sanchez-Yamagishi, J. D.; Watanabe, K.; Taniguchi, T.; Kaxiras, E.; et al. Correlated insulator behaviour at half-filling in magic-angle graphene superlattices. *Nature* **2018**, *556* (7699), 80−84.

(5) Sharpe, A. L.; Fox, E. J.; Barnard, A. W.; Finney, J.; Watanabe, K.; Taniguchi, T.; Kastner, M. A.; Goldhaber-Gordon, D. Emergent ferromagnetism near three-quarters filling in twisted bilayer graphene. *Science* **2019**, *365* (6453), 605−608.

(6) Cao, Y.; Rodan-Legrain, D.; Rubies-Bigorda, O.; Park, J. M.; Watanabe, K.; Taniguchi, T.; Jarillo-Herrero, P. Tunable correlated states and spin-polarized phases in twisted bilayer−bilayer graphene. *Nature* **2020**, *583* (7815), 215−220.

(7) Serlin, M.; Tschirhart, C. L.; Polshyn, H.; Zhang, Y.; Zhu, J.; Watanabe, K.; Taniguchi, T.; Balents, L.; Young, A. F. Intrinsic quantized anomalous Hall effect in a moiré heterostructure. *Science* **2020**, *367* (6480), 900−903.

(8) Cao, Y.; Rodan-Legrain, D.; Park, J. M.; Yuan, N. F. Q.; Watanabe, K.; Taniguchi, T.; Fernandes, R. M.; Fu, L.; Jarillo-Herrero, P. Nematicity and competing orders in superconducting magic-angle graphene. *Science* **2021**, *372* (6539), 264−271.

(9) Cao, Y.; Park, J. M.; Watanabe, K.; Taniguchi, T.; Jarillo-Herrero, P. Pauli-limit violation and re-entrant superconductivity in moiré graphene. *Nature* **2021**, *595* (7868), 526−531.

(10) Huang, D.; Choi, J.; Shih, C.-K.; Li, X. Excitons in semiconductor moiré superlattices. *Nat. Nanotechnol.* **2022**, *17* (3), 227−238.

(11) Duan, S.; Cui, Y.; Yi, W.; Chen, X.; Yang, B.; Liu, X. Enhanced Thermoelectric Performance in Black Phosphorene via Tunable Interlayer Twist. *Small* **2022**, *18* (49), No. 2204197.

(12) Fang, T.; Liu, T.; Jiang, Z.; Yang, R.; Servati, P.; Xia, G. Fabrication and the Interlayer Coupling Effect of Twisted Stacked Black Phosphorus for Optical Applications. *ACS Appl. Nano Mater.* **2019**, *2* (5), 3138−3145.

(13) Lv, M.; Sun, X.; Chen, Y.; Taniguchi, T.; Watanabe, K.; Wu, M.; Wang, J.; Xue, J. Spatially Resolved Polarization Manipulation of Ferroelectricity in Twisted hBN. *Adv. Mater.* **2022**, *34* (51), No. 2203990.

(14) Chiodini, S.; Kerfoot, J.; Venturi, G.; Mignuzzi, S.; Alexeev, E. M.; Teixeira Rosa, B.; Tongay, S.; Taniguchi, T.; Watanabe, K.; Ferrari, A. C.; Ambrosio, A. Moiré Modulation of Van Der Waals Potential in Twisted Hexagonal Boron Nitride. *ACS Nano* **2022**, *16* (5), 7589−7604.

(15) Gao, X.-G.; Li, X.-K.; Xin, W.; Chen, X.-D.; Liu, Z.-B.; Tian, J.-G. Fabrication, optical properties, and applications of twisted two-dimensional materials. *Nanophotonics* **2020**, *9* (7), 1717−1742.

(16) Foutty, B. A.; Kometter, C. R.; Devakul, T.; Reddy, A. P.; Watanabe, K.; Taniguchi, T.; Fu, L.; Feldman, B. E. Mapping twist-tuned multiband topology in bilayer WSe_2. *Science* **2024**, *384* (6693), 343−347.

(17) Regan, E. C.; Wang, D.; Jin, C.; Utama, M. I. B.; Gao, B.; Wei, X.; Zhao, S.; Zhao, W.; Zhang, Z.; Yumigeta, K.; et al. Mott and generalized Wigner crystal states in WSe_2/WS_2 moiré superlattices. *Nature* **2020**, *579* (7799), 359−363.

(18) Wu, F.; Lovorn, T.; Tutuc, E.; Martin, I.; MacDonald, A. H. Topological Insulators in Twisted Transition Metal Dichalcogenide Homobilayers. *Phys. Rev. Lett.* **2019**, *122* (8), No. 086402.

(19) An, L.; Cai, X.; Pei, D.; Huang, M.; Wu, Z.; Zhou, Z.; Lin, J.; Ying, Z.; Ye, Z.; Feng, X.; et al. Interaction effects and superconductivity signatures in twisted double-bilayer WSe_2. *Nanoscale Horiz.* **2020**, *5* (9), 1309−1316.

(20) Wang, S.; Cui, X.; Jian, Ce.; Cheng, H.; Niu, M.; Yu, J.; Yan, J.; Huang, W. Stacking-Engineered Heterostructures in Transition Metal Dichalcogenides. *Adv. Mater.* **2021**, *33* (16), No. 2005735.

(21) Xian, L.; Kennes, D. M.; Tancogne-Dejean, N.; Altarelli, M.; Rubio, A. Multiflat Bands and Strong Correlations in Twisted Bilayer Boron Nitride: Doping-Induced Correlated Insulator and Superconductor. *Nano Lett.* **2019**, *19* (8), 4934−4940.

(22) Xu, Y.; Ray, A.; Shao, Y.-T.; Jiang, S.; Lee, K.; Weber, D.; Goldberger, J. E.; Watanabe, K.; Taniguchi, T.; Muller, D. A.; et al. Coexisting ferromagnetic−antiferromagnetic state in twisted bilayer CrI_3. *Nat. Nanotechnol.* **2022**, *17* (2), 143−147.

(23) Jang, M.; Lee, S.; Cantos-Prieto, F.; Košić, I.; Li, Y.; McCray, A. R. C.; Jung, M.-H.; Yoon, J.-Y.; Boddapati, L.; Deepak, F. L.; et al. Direct observation of twisted stacking domains in the van der Waals magnet CrI_3. *Nat. Commun.* **2024**, *15* (1), No. 5925.

(24) Yang, B.; Patel, T.; Cheng, M.; Pichugin, K.; Tian, L.; Sherlekar, N.; Yan, S.; Fu, Y.; Tian, S.; Lei, H.; et al. Macroscopic tunneling probe of Moiré spin textures in twisted CrI_3. *Nat. Commun.* **2024**, *15* (1), No. 4982.

(25) Xie, H.; Luo, X.; Ye, G.; Ye, Z.; Ge, H.; Sung, S. H.; Rennich, E.; Yan, S.; Fu, Y.; Tian, S.; et al. Twist engineering of the two-dimensional magnetism in double bilayer chromium triiodide homostructures. *Nat. Phys.* **2022**, *18* (1), 30−36.

(26) Akram, M.; Kapeghian, J.; Das, J.; Valentí, R.; Botana, A. S.; Erten, O. Theory of Moiré Magnetism in Twisted Bilayer α-$RuCl_3$. *Nano Lett.* **2024**, *24* (3), 890−896.

(27) Yao, F.; Rossi, D.; Gabrovski, I. A.; Multian, V.; Hua, N.; Watanabe, K.; Taniguchi, T.; Gibertini, M.; Gutiérrez-Lezama, I.; Rademaker, L.; Morpurgo, A. F. Moiré magnetism in $CrBr_3$ multilayers emerging from differential strain. *Nat. Commun.* **2024**, *15* (1), No. 10377.

(28) Qiao, L.-Y.; Jiang, X.-C.; Ruan, Z.; Zhang, Y.-Z. Tunable magnetism in bilayer transition metal dichalcogenides. *Phys. Rev. Mater.* **2024**, *8* (3), No. 034003.

(29) Liu, Y.; Yu, J.; Liu, C.-C. Twisted Magnetic Van der Waals Bilayers: An Ideal Platform for Altermagnetism. *Phys. Rev. Lett.* **2024**, *133* (20), No. 206702.

(30) Sheoran, S.; Bhattacharya, S. Nonrelativistic spin splittings and altermagnetism in twisted bilayers of centrosymmetric antiferromagnets. *Phys. Rev. Mater.* **2024**, *8* (5), No. L051401.

(31) Yang, W.; Yang, X.; Li, M.; Hu, L.; Zheng, F. Interlayer magnetic interactions and ferroelectricity in $\pi/3$-twisted CrX_2 (X = Se, Te) bilayers. *Appl. Phys. Lett.* **2024**, *124* (2), No. 021901.

(32) Boix-Constant, C.; Jenkins, S.; Rama-Eiroa, R.; Santos, E. J. G.; Mañas-Valero, S.; Coronado, E. Multistep magnetization switching in orthogonally twisted ferromagnetic monolayers. *Nat. Mater.* **2024**, *23* (2), 212−218.

(33) Sboychakov, A. O.; Rozhkov, A. V.; Rakhmanov, A. L.; Nori, F. Externally Controlled Magnetism and Band Gap in Twisted Bilayer Graphene. *Phys. Rev. Lett.* **2018**, *120* (26), No. 266402.

(34) Cheng, G.; Rahman, M. M.; Allcca, A. L.; Rustagi, A.; Liu, X.; Liu, L.; Fu, L.; Zhu, Y.; Mao, Z.; Watanabe, K.; et al. Electrically tunable moiré magnetism in twisted double bilayers of chromium triiodide. *Nat. Electron.* **2023**, *6* (6), 434−442.

(35) Pacchioni, G. Switching moiré magnets. *Nat. Rev. Mater.* **2024**, *9* (7), 454.

(36) Yang, B.; Patel, T.; Cheng, M.; Pichugin, K.; Tian, L.; Sherlekar, N.; Yan, S.; Fu, Y.; Tian, S.; Lei, H.; et al. Macroscopic tunneling probe of Moiré spin textures in twisted CrI_3. *Nat. Commun.* **2024**, *15* (1), No. 4982.

(37) Yu, J.; Liu, D.; Ding, Z.; Yuan, Y.; Zhou, J.; Pei, F.; Pan, H.; Ma, T.; Jin, F.; Wang, L.; et al. Direct Imaging of Antiferromagnet-Ferromagnet Phase Transition in van der Waals Antiferromagnet CrSBr. *Adv. Funct. Mater.* **2024**, *34* (2), No. 2307259.

(38) Boix-Constant, C.; Rybakov, A.; Miranda-Pérez, C.; Martínez-Carracedo, G.; Ferrer, J.; Mañas-Valero, S.; Coronado, E. Programmable Magnetic Hysteresis in Orthogonally-Twisted 2D CrSBr Magnets via Stacking Engineering. *Adv. Mater.* **2025**, *37* (8), No. 2415774.

(39) Bagani, K.; Vervelaki, A.; Jetter, D.; Devarakonda, A.; Tschudin, M. A.; Gross, B.; Chica, D. G.; Broadway, D. A.; Dean, C. R.; Roy, X.; et al. Imaging Strain-Controlled Magnetic Reversal in Thin CrSBr. *Nano Lett.* **2024**, *24* (41), 13068−13074.

(40) Wang, B.; Wu, Y.; Bai, Y.; Shi, P.; Zhang, G.; Zhang, Y.; Liu, C. Origin and regulation of triaxial magnetic anisotropy in the ferromagnetic semiconductor CrSBr monolayer. *Nanoscale* **2023**, *15* (32), 13402−13410.

(41) Wang, H.; Qi, J.; Qian, X. Electrically tunable high Curie temperature two-dimensional ferromagnetism in van der Waals layered crystals. *Appl. Phys. Lett.* **2020**, *117* (8), No. 083102.

(42) Yang, K.; Wang, G.; Liu, L.; Lu, D.; Wu, H. Triaxial magnetic anisotropy in the two-dimensional ferromagnetic semiconductor CrSBr. *Phys. Rev. B* **2021**, *104* (14), No. 144416.

(43) Huang, B.; Clark, G.; Navarro-Moratalla, E.; Klein, D. R.; Cheng, R.; Seyler, K. L.; Zhong, D.; Schmidgall, E.; McGuire, M. A.; Cobden, D. H.; et al. Layer-dependent ferromagnetism in a van der Waals crystal down to the monolayer limit. *Nature* **2017**, *546* (7657), 270−273.

(44) Gong, C.; Li, L.; Li, Z.; Ji, H.; Stern, A.; Xia, Y.; Cao, T.; Bao, W.; Wang, C.; Wang, Y.; et al. Discovery of intrinsic ferromagnetism in two-dimensional van der Waals crystals. *Nature* **2017**, *546* (7657), 265−269.

(45) Telford, E. J.; Dismukes, A. H.; Lee, K.; Cheng, M.; Wieteska, A.; Bartholomew, A. K.; Chen, Y.-S.; Xu, X.; Pasupathy, A. N.; Zhu, X.; et al. Layered Antiferromagnetism Induces Large Negative Magnetoresistance in the van der Waals Semiconductor CrSBr. *Adv. Mater.* **2020**, *32* (37), No. 2003240.

(46) Guo, H.-T.; Guo, S.-D.; Ang, Y. S. Electric-field induced half-metallic properties in an experimentally synthesized CrSBr monolayer. *Phys. Chem. Chem. Phys.* **2023**, *25* (44), 30269−30275.

(47) Diao, Y.; Jin, C.; Gu, X.; Lu, Z.; Zhang, J.; Dong, Z.; Liu, D.; Fu, H.; Zhong, C. Strain-regulated magnetic phase transition and perpendicular magnetic anisotropy in CrSBr monolayer. *Phys. E* **2023**, *147*, No. 115590.

(48) Sahu, S.; Volochanskyi, O.; Varade, V.; Pirker, L.; Zólyomi, V.; Koltai, J.; Mosina, K.; Sofer, Z.; Frank, O.; Vejpravová, J.; et al. Tuning of MoS_2 Photoluminescence in Heterostructures with CrSBr. *ACS Appl. Mater. Interfaces* **2025**, *17* (17), 25693−25701.

(49) Zhou, X.; Li, M.; Zhou, B. Raising the Curie Temperature of Two-Dimensional Semiconducting CrSbr by van der Waals Coupling with In-Plane Ferroelectric GeS. *J. Phys. Chem. C* **2024**, *128* (45), 19398−19409.

(50) Wang, L. Beyond moiré in twisted two-dimensional magnets. *Nat. Mater.* **2024**, *23* (2), 174−175.

(51) Chen, Y.; Samanta, K.; Shahed, N. A.; Zhang, H.; Fang, C.; Ernst, A.; Tsymbal, E. Y.; Parkin, S. S. P. Twist-assisted all-antiferromagnetic tunnel junction in the atomic limit. *Nature* **2024**, *632* (8027), 1045−1051.

(52) Liu, J.; Zhang, X.; Lu, G. Moiré magnetism and moiré excitons in twisted CrSBr bilayers. *Proc. Natl. Acad. Sci. U.S.A.* **2025**, *122* (1), No. e2413326121.

(53) Jin, C.; Ma, E. Y.; Karni, O.; Regan, E. C.; Wang, F.; Heinz, T. F. Ultrafast dynamics in van der Waals heterostructures. *Nat. Nanotechnol.* **2018**, *13* (11), 994−1003.

(54) Kresse, G.; Furthmuller, J. Efficiency of Ab-Initio Total Energy Calculations for Metals and Semiconductors Using a Plane-Wave Basis Set. *Comput. Mater. Sci.* **1996**, *6* (1), 15−50.

(55) Kresse, G.; Furthmüller, J. Efficient iterative schemes for ab initio total-energy calculations using a plane-wave basis set. *Phys. Rev. B* **1996**, *54* (16), 11169−11186.

(56) Perdew, J. P.; Burke, K.; Ernzerhof, M. Generalized Gradient Approximation Made Simple. *Phys. Rev. Lett.* **1996**, *77* (18), No. 3865.

(57) Li, M.; Zhou, B. Adjustable Electronic Properties of Two-Dimensional Ferromagnetic Semiconductor CrSBr by van der Waals Interfacial Coupling. *J. Phys. Chem. C* **2023**, *127* (45), 22378−22386.

(58) Hou, C.; Wang, X.; Sun, Y.; Lu, Y.; Ni, J. Magnetic−Electronic Coupling in the Strained Bilayer CrSBr. *J. Phys. Chem. C* **2023**, *127* (46), 22833−22841.

(59) Bo, X.; Li, F.; Xu, X.; Wan, X.; Pu, Y. Calculated magnetic exchange interactions in the van der Waals layered magnet CrSBr. *New J. Phys.* **2023**, *25* (1), No. 013026.

(60) Grimme, S.; Antony, J.; Ehrlich, S.; Krieg, H. A consistent and accurate ab initio parametrization of density functional dispersion correction (DFT-D) for the 94 elements H-Pu. *J. Chem. Phys.* **2010**, *132* (15), No. 154104.

(61) Monkhorst, H. J.; Pack, J. D. Special points for Brillouin-zone integrations. *Phys. Rev. B* **1976**, *13* (12), 5188−5192.

(62) Togo, A.; Tanaka, I. First Principles Phonon Calculations in Materials Science. *Scr. Mater.* **2015**, *108*, 1−5.

(63) Wang, V.; Xu, N.; Liu, J.-C.; Tang, G.; Geng, W.-T. VASPKIT: A user-friendly interface facilitating high-throughput computing and analysis using VASP code. *Comput. Phys. Commun.* **2021**, *267*, No. 108033.

(64) Delley, B. An all-electron numerical method for solving the local density functional for polyatomic molecules. *J. Chem. Phys.* **1990**, *92* (1), 508−517.

(65) Delley, B. From molecules to solids with the $DMol_3$ approach. *J. Chem. Phys.* **2000**, *113* (18), 7756−7764.

(66) Beck, J. Über Chalkogenidhalogenide des Chroms Synthese, Kristallstruktur und Magnetismus von Chromsulfidbromid, CrSBr. *Z. Anorg. Allg. Chem.* **1990**, *585* (1), 157−167.

(67) dos Santos, J. M. B. L.; Peres, N. M. R.; Neto, A. H. C. Graphene Bilayer with a Twist: Electronic Structure. *Phys. Rev. Lett.* **2007**, *99* (25), No. 256802.

(68) Naik, M. H.; Jain, M. Ultraflatbands and Shear Solitons in Moire Patterns of Twisted Bilayer Transition Metal Dichalcogenides. *Phys. Rev. Lett.* **2018**, *121* (26), No. 266401.

(69) Chen, W.; Sun, Z.; Wang, Z.; Gu, L.; Xu, X.; Wu, S.; Gao, C. Direct observation of van der Waals stacking−dependent interlayer magnetism. *Science* **2019**, *366* (6468), 983−987.

(70) Lee, K.; Dismukes, A. H.; Telford, E. J.; Wiscons, R. A.; Wang, J.; Xu, X.; Nuckolls, C.; Dean, C. R.; Roy, X.; Zhu, X. Magnetic Order and Symmetry in the 2D Semiconductor CrSBr. *Nano Lett.* **2021**, *21* (8), 3511−3517.

(71) Zhang, F.; Lv, L.; Xu, Z.; Qi, D.; Wang, W.; Li, X.; Su, Y.; Jiang, Y.; Guan, Z. Prediction of the TiS_2 Bilayer with Self-Intercalation: Robust Ferromagnetic Semiconductor with a High Curie Temperature. *J. Phys. Chem. C* **2025**, *129* (11), 5577−5588.

(72) Wang, D.-s.; Wu, R.; Freeman, A. J. First-Principles Theory of Surface Magnetocrystalline Anisotropy and the Diatomic-Pair Model. *Phys. Rev. B* **1993**, *47*, No. 14932.

(73) Dirnberger, D.; Kresse, G.; Franchini, C.; Reticcioli, M. Electronic State Unfolding for Plane Waves: Energy Bands, Fermi Surfaces, and Spectral Functions. *J. Phys. Chem. C* **2021**, *125* (23), 12921−12928.

(74) Huang, S.; Yu, B.; Ma, Y.; Pan, C.; Ma, J.; Zhou, Y.; Ma, Y.; Yang, K.; Wu, H.; Lei, Y.; et al. Bright dipolar excitons in twisted black phosphorus homostructures. *Science* **2024**, *386* (6721), 526−531.

(75) Tebyetekerwa, M.; Truong, T. N.; Yan, W.; Tang, C.; Wibowo, A. A.; Bullock, J.; Du, A.; Yan, C.; Macdonald, D.; Nguyen, H. T. Twist Angle Effects on the Absorbance, Carrier Lifetime, and Diffusion Properties in Low Dimension Type-II MoS_2/WS_2 Heterobilayers. *Adv. Mater. Interfaces* **2022**, *9* (34), No. 2201649.